Journal of Materials Chemistry A

ROYAL SOCIETY OF CHEMISTRY

PAPER

View Article Online
View Journal | View Issue

Check for updates

Cite this: J. Mater. Chem. A, 2025, 13, 38908

Maximizing oxygen permeation *via* catalytic functionalization under oxyfuel conditions

Laura Almar,[a] Julio Garcia-Fayos,[a] Rian Ruhl,[b] Laura Navarrete,[a] Maria Balaguer,[a] Marwan Laqdiem,[a] Jong Hoon Joo,[c] Henny J. M. Bouwmeester[b] and José M. Serra*[a]

Received 11th August 2025
Accepted 20th October 2025

DOI: 10.1039/d5ta06504f

rsc.li/materials-a

Oxygen transport membranes (OTMs) offer a promising route for high-efficiency, cost-effective oxygen supply in energy and chemical industries, with the potential to significantly reduce CO_2 and NO_x emissions when integrated into oxy-combustion processes. However, conventional OTMs suffer from poor chemical stability in CO_2-rich environments, prompting the development of dual-phase membranes that, while more stable, typically exhibit lower oxygen permeation rates. In this study, we address this limitation by enhancing the surface exchange kinetics of Fe_2NiO_4–$Ce_{0.8}Tb_{0.2}O_{2-\delta}$ (NFO–CTO) membranes by surface modification with various oxygen oxidation–reduction reaction (OORR) catalysts, including Ce, Pr, Sm, Tb, Co, Nb, Zr, and Al oxides, and Pr-based binary oxides. Comprehensive characterization using electrochemical impedance spectroscopy, oxygen isotopic exchange, and gas permeation measurements revealed a substantial improvement in surface reaction kinetics. Catalyst activation led to a six-fold increase in oxygen flux under standard conditions and up to a 2.5-fold enhancement under harsh environments containing CO_2 and SO_2 at 850 °C, mimicking oxyfuel combustion conditions. This work demonstrates that rational catalyst selection and integration can overcome fundamental surface limitations in dual-phase membranes, offering a viable strategy to advance oxygen separation technologies for sustainable energy applications.

1. Introduction

Power generation and industry sectors account for more than 42% of global CO_2 emissions. In 2023, global CO_2 emissions from these sectors reached around 34.5 Gt ($GtCO_2$), with a year-on-year increase of about 0.9%. Although this is a slight improvement from previous years, the upward trend continues due to persistent demand for energy, particularly in regions like Asia.[1–3] Amongst the existing technologies, oxyfuel combustion (fuel combustion with pure O_2) is a leading option for implementing carbon capture and storage (CCS) strategies. This process enhances CO_2 capture efficiency by producing a flue gas that consists mostly of CO_2 and water, making CO_2 separation easier.[4,5] With regard to the O_2 supply, the use of Oxygen Transport Membrane (OTM) modules offers an alternative to traditional cryogenic O_2 production,[6] permitting its integration into most existing medium-to-small scale installations as a promising and cost-effective solution.[7–11]

In recent years, significant advances have been made in producing CO_2- and SO_2-stable mixed ionic-electronic conducting (MIEC) materials for oxyfuel applications.[12–16] One of the most promising approaches is the use of dual-phase composites that integrate an electronic conductor with an ionic conductor, such as Fe_2NiO_4–$Ce_{0.8}Tb_{0.2}O_{2-\delta}$, $Ce_{0.8}Gd_{0.2}O_{2-\delta}$–$FeCo_2O_4$, $Ce_{0.8}Gd_{0.15}Cu_{0.05}O_{2-\delta}$–$SrFeO_{3-\delta}$, $Ce_{0.85}Gd_{0.1}Cu_{0.05}O_{2-\delta}$–$La_{0.6}Ca_{0.4}FeO_{3-\delta}$. Particularly, the 60% Fe_2NiO_4–40% $Ce_{0.8}Tb_{0.2}O_{2-\delta}$ (NFO–CTO) system[17–20] presented outstanding stability and high performance. However, the obtained oxygen permeability should be further improved to meet the techno-economic target of 10 ml min^{-1} cm^{-2}.[18] To approach this goal, membrane thickness can be reduced; for instance, high O_2 permeation was achieved under oxyfuel conditions using a 10 μm-thick NFO–CTO membrane.[17] Since reducing thickness increases the influence of surface exchange reactions on oxygen permeability, additional surface modifications can be employed to further enhance oxygen flux, particularly when surface exchange becomes the rate-limiting step.[21,22] This limitation is particularly significant at lower temperatures or when the membrane thickness is reduced.[23] One common approach to improving surface exchange reactions and increasing the oxygen flux is the addition of porous layers to the membrane surface, consisting of the same dual-phase material with the same or different ratios, or a new material.[24–26] These

[a]Instituto de Tecnología Química (Universitat Politècnica de València – Consejo Superior de Investigaciones Científicas), 46022 Valencia, Spain. E-mail: jmserra@itq.upv.es

[b]Electrochemistry Research Group, Faculty of Science and Technology, MESA+ Institute for Nanotechnology, University of Twente, The Netherlands

[c]Department of Environment and Energy Engineering, Gwangju Institute of Science and Technology, Gwangju 61005, Republic of Korea

modifications primarily boost oxygen permeation by increasing the surface-specific area, providing more active sites, and extending the triple phase boundary (TPB) where the oxygen oxidation/reduction reaction (OORR) takes place. However, the performance of these systems remains limited by the reaction kinetics involved in the adsorption, dissociation, and recombination of oxygen. Adding active elements with redox properties and strong adsorption capabilities can enhance these surface exchange reactions, improving O_2 permeation. Several lanthanide and metal oxides are candidates that could meet these criteria.[27–29] In this work, a screening study was carried out to evaluate the catalytic activation of porous NFO–CTO layers with different single-element oxides and Pr-based binary formulations. These elements were selected based on their reported ability to enhance surface oxygen exchange kinetics (*e.g.*, Ce, Pr, Sm, Tb *via* high oxygen mobility and redox activity), provide electronic conductivity and catalytic sites (*e.g.*, Co), or improve structural and chemical stability under reactive environments (*e.g.*, Nb, Zr, Al). The catalytic performance was assessed by electrochemical impedance spectroscopy and isotopic exchange to quantify improvements in surface exchange kinetics and oxygen ion transport. These kinetic parameters were then correlated with oxygen permeation measurements to establish structure–property relationships and identify the most effective catalytic promoters.

2. Material and methods

2.1. Materials and membranes fabrication

NFO–CTO (60% Fe_2NiO_4–40% $Ce_{0.8}Tb_{0.2}O_{2-\delta}$) composite powders were synthesized by a one-pot Pechini method. To this end, stoichiometric amounts of metal nitrates ($Ce(NO_3)_3\cdot 6H_2O$, and $Fe(NO_3)_3\cdot 9H_2O$ provided by Sigma Aldrich, $Tb(NO_3)_3\cdot 6H_2O$, and $Ni(NO_3)_3\cdot 6H_2O$ by ABCR GmbH) were dissolved in distilled water. Subsequently, citric acid (Sigma Aldrich) and ethylene glycol were added as chelating and gelating agents in a molar ratio of metal : citric acid : ethylene glycol 1 : 2 : 4. After drying up to 270 °C, the obtained gel was fired at 600 °C to obtain finely dispersed powders with the correct crystalline phases. Dense NFO–CTO ceramics were obtained by uniaxial pressing, followed by sintering of the obtained disks in air at 1400 °C for 10 h (2 °C min^{-1} heating rate, 5 °C min^{-1} cooling rate). For oxygen permeation measurements, membranes with a diameter of 15 mm and a thickness of 0.6 mm were obtained from the sintered NFO–CTO disks after grinding and polishing with sandpaper.

$Ce_{0.8}Gd_{0.2}O_{1.9}$ (CGO) dense electrolytes were selected for electrochemical impedance spectroscopy (EIS) studies. The CGO powders were synthesized using the co-precipitation method and co-doped with cobalt to improve sinterability.[30,31] This was done by impregnating a 2% molar of $Co(NO_3)_2\cdot 6H_2O$ dissolved in deionized water. The obtained powders were calcined in air at 800 °C for 5 h. Dense disks (CGO-Co) were obtained by uniaxial pressing, followed by sintering in air at 1480 °C for 4 h (2 °C min^{-1} heating rate, 5 °C min^{-1} cooling rate). The densities of all samples, checked by Archimedes' method and SEM, exceeded 98%.

For EIS and oxygen permeation measurements, 30 μm-thick porous layers of NFO–CTO were screen-printed on both sides of CGO electrolyte disks and NFO–CTO membranes, respectively. Inks for screen-printing were made by mixing NFO–CTO and terpineol in a 1 : 2 weight ratio in a three-roll mill. After deposition, the obtained samples were sintered in air at 1100 °C for 2 h. Catalytic activation of the porous NFO–CTO scaffold layers was accomplished by infiltration of well-dispersed catalyst nanoparticles. To this end, 2 M solutions of the element precursors Ce, Pr, Sm, Tb, Co, Nb, Zr, and Al oxides and Pr-based binary formulations (typically nitrates) were prepared in a 1 : 1 ethanol–water volume ratio and dripped onto the porous composite scaffold layers.[32] After infiltration by capillary force, the samples were dried at 80 °C for 1 h and calcined in air at 850 °C for 2 h.

NFO–CTO composite powders for Pulse Isotopic Exchange (PIE) measurements were obtained by crushing dense sintered samples, and sieving the obtained powder through a 100 μm mesh. These composite powders were activated with catalyst nanoparticles by incipient wetness impregnation using the abovementioned procedure. Ce, Pr, Al, Ce–Pr, and Pr–Al cations were selected as representative catalysts based on the screening results obtained from the EIS study.

2.2. Membrane characterization

The crystalline phases of the prepared samples were identified by using a PANalytical Cubix fast diffractometer with CuKα1 radiation ($\lambda = 1.5406$ Å) and an X'Celerator detector, operating in Bragg–Brentano geometry. X-ray diffraction (XRD) patterns recorded in the 2θ range from 25° to 90° were analyzed using X'Pert Highscore Plus software. Cross-sectional analysis of the sintered samples, both before and after the tests, was conducted by performing scanning electron microscopy (SEM) and energy dispersive X-ray (EDX) characterization using a ZEISS Ultra55 field emission scanning electron microscope. Additionally, backscattered detector (BSD) imaging was used to provide compositional contrast for distinguishing grains and elemental distributions.

PIE measurements were conducted using a homemade setup described elsewhere.[33] The powder samples were loaded in the centre of a quartz tubular micro-reactor with an inner diameter of 2 mm. Quartz wool plugs were used to secure the packed powder bed. The length and mass of the packed bed were typically 10 mm and 0.08 g, respectively. $^{16}O_2$ mixed with Ar was used as carrier gas and fed through the reactor with a total flow rate of 30 ml min^{-1} (NTP). Gases were dried using Agilent gas clean moisture filters before entering the reactor. Oxygen isotope gas was purchased from Cambridge Isotope Laboratories, Inc. (>97 atom% $^{18}O_2$). A six-port valve with a 500 μl sample loop was used for injection of the $^{18}O_2/N_2$ pulse into the $^{16}O_2$/Ar carrier gas, with the pulse having the same pO_2 as the carrier gas. The diluent N_2 in the pulse was used for internal calibration of the mass spectrometer (Omni Star TM GSD 301 Pfeiffer-Vacuum). The mean residence time of the reactor varied between 10 and 30 ms, depending on temperature. Prior to measurements, the samples were pre-treated at 850 °C for 2 h to

remove possibly adsorbed water and CO_2, then cooled to 50 °C at a rate of 5 °C min^{-1}. Measurements were performed at a pO_2 of 0.21 atm. Averaged values of the $^{18}O_2$ and $^{16}O^{18}O$ effluent fractions in three pulse experiments, at a given temperature, were used to calculate the exchange rate. The reactor was equilibrated prior to each measurement before data acquisition. The overall surface exchange rate, $\mathscr{R}_0$ [mol (O) m^{-2} s^{-1}], was calculated from:

$$\mathscr{R}_0 = \frac{2F_m}{S} \ln\left(\frac{f_i^{18}}{f_e^{18}}\right) \quad (1)$$

where f_i^{18} and f_e^{18} are the ^{18}O isotope fractions in the pulse at the reactor's inlet and outlet, respectively, F_m is the molar flow rate of oxygen through the packed bed, and S is the total surface area of the sample. The fraction f^{18} was calculated from:

$$f^{18} = 0.5f^{34} + f^{36} \quad (2)$$

Symmetrical NFO–CTO/CGO/NFO–CTO cells for impedance measurements were prepared by coating 30 μm-thick porous NFO–CTO layers, with and without catalyst-impregnation, onto both sides of 0.8 mm-thick CGO-Co electrolyte disks. Measurements were performed with an excitation voltage of 20 mV in the frequency range 0.01–3 × 10^5 Hz, using a Solartron 1470E multichannel potentiostat and a 1455A frequency response analyzer. Measurements were performed at 850 °C, under different atmospheres (air, 5% O_2 in N_2, 5% O_2 in CO_2, and 250 ppm in 5% O_2 in CO_2). In all cases, the total flow remained constant (100 ml min^{-1}). The impedance spectra were analysed using ZView2® software. The impedance spectra were fitted using the equivalent circuit $LR_e(R_1Q_1)(R_2Q_2)(R_3Q_3)$, where L is an inductance, R_e the apparent ohmic resistance, R_i (i = 1, 2, 3) the different contributions of the total polarization resistance (R_P), and Q_i (i = 1, 2, 3) the corresponding constant phase element. Table 1 presents the various test environments and durations analyzed using electrochemical impedance spectroscopy (EIS).

Permeation tests were performed on a gastight NFO–CTO composite disk sintered at 1400 °C for 10 h, resulting in a final membrane thickness of 0.6 mm. NFO–CTO membranes were screen-printed on both sides with a 30 μm-thick porous NFO–CTO layer. After deposition and drying, the layers were calcined at 1100 °C in air for 2 h. The permeation tests were conducted in a lab-scale reactor consisting of a cylindrical two chambers quartz reactor, in which synthetic air (21%, vol. O_2) was fed into the oxygen-rich chamber, while Ar, 30% vol. CO_2 in Ar and 250 ppm SO_2 in 30% vol. CO_2 in Ar were used as sweep gases on the permeate side chamber, in a 4-end mode configuration. Both streams were fed at atmospheric pressure. Inlet gases were preheated in order to ensure proper contact temperature with the membrane surface. This is particularly important when high gas flow rates are employed. All streams were individually controlled by mass flow controllers. The temperature was measured by a thermocouple attached to the membrane. Membrane gas leak-free conditions were achieved using rings of tailored alloys. The permeate was analyzed at steady state by online gas chromatography using a micro-GC Varian CP-4900 equipped with Molsieve5A, Pora-Plot-Q glass capillary, and CP-Sil modules. Leak-tight sealing and membrane integrity were ensured by continuously monitoring the N_2 concentration in the product gas stream. Sealing was considered acceptable when the ratio between the oxygen flow leak and the oxygen flux remained lower than 3%. The reported data were collected at steady state after at least 1 h in the reaction stream. Each test was repeated three times, yielding an analytical error below 0.5%.

3. Results and discussion

3.1. Structural characterization

XRD patterns of the impregnated NFO–CTO catalytic powders are presented in the SI. These powders were subjected to the same thermal cycling and catalyst loading as the infiltrated porous NFO–CTO backbones used in electrochemical impedance spectroscopy, oxygen isotopic exchange, and gas permeation measurements.

Peaks associated with the NFO–CTO phase, along with peaks associated with the different oxide catalysts, are visible in the XRD patterns. Fig. S1 shows characteristic peaks for NFO–CTO powders with ZrO_2, Co_3O_4, Tb_7O_{12}, Sm_2O_3, and Nb_2O_3, while Fig. S2 shows peaks for NFO–CTO powders with CeO_2, Pr_6O_{11}, Al_2O_3, Pr–Al, Ce–Pr. In the particular cases of Al, Ce, and Ce–Pr catalysts, it was not possible to detect the corresponding oxide catalyst phase(s). On the one hand, the resulting catalyst oxide particles could be CeO_2 and CeO_2-PrO_2, masked by the CTO fluorite phase from the backbone, or the concentration of catalyst nanoparticles being below the detection limit of XRD.

Scanning Electron Microscopy (SEM) cross-sectional images of the NFO–CTO backbone and all the infiltrated NFO–CTO backbones (Co, Sm, Al, Nb, Tb, Zr, Ce, Pr, Ce–Pr, and Pr–Al) after calcination in air at 850 °C are shown in Fig. 1. A good dispersion of the composite particles in the backbone is easily identifiable in the backscattered detector (BSD) image, with NFO appearing as dark grey and CTO as light grey, indicating a well-

Table 1 EIS test conditions studied for the different symmetrical NFO–CTO/CGO/NFO–CTO cells

	Gas composition	Duration
Feed side	21% O_2 in N_2	90 min
Sweep side (clean conditions)	5% O_2 in N_2	90 min
Sweep side (oxyfuel conditions)	5% O_2 in CO_2	90 min
Sweep side (oxyfuel conditions)	250 ppm SO_2, 5% O_2 in CO_2	250 min
Sweep side (recovery, clean conditions)	5% O_2 in N_2	10 h

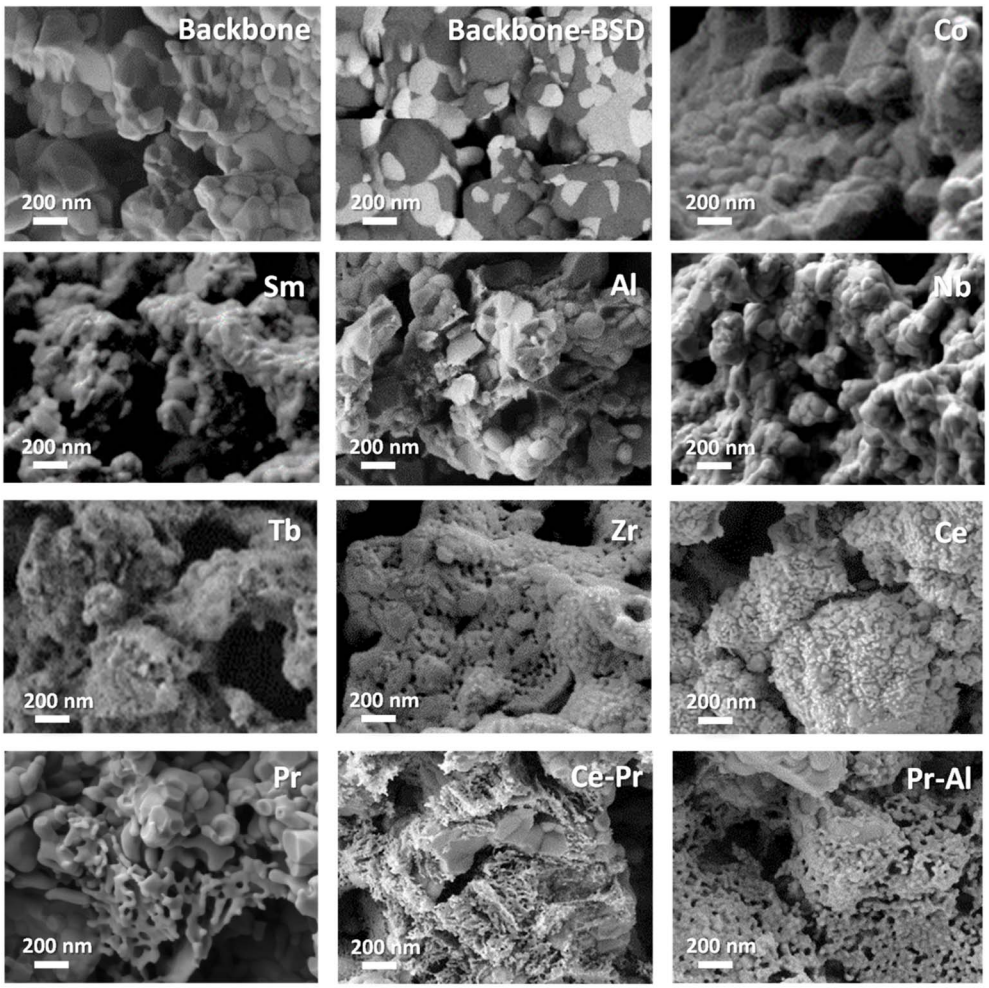

Fig. 1 SEM and BSD cross-sectional images of a pure NFO–CTO backbone and infiltrated (Co, Sm, Al, Nb, Tb, Zr, Ce, Pr, Ce–Pr, and Pr–Al) NFO–CTO backbones after sintering at 850 °C.

distributed composition and rounded particle morphology. Furthermore, nano-sized catalyst particles showed different particle morphologies with particle sizes below 100 nm, depending on the specific infiltrated metal oxide. Most catalyst particles show spherical morphology, whereas Pr_6O_{11} and Al_2O_3 show needle- and sheet-like morphologies, respectively.

3.2. Electrochemical characterization

The electrochemical performance of the different backbones with and without catalyst activation on CGO-Co electrolytes was studied at 850 °C in streams of 21% O_2 in N_2 and 5% O_2 in N_2, mimicking feed and clean sweep side environments, respectively. Fig. 2 shows the total polarization resistance (R_p) values obtained for each catalytically-activated membrane after 90 min on-stream under both conditions (21% O_2 and 5% O_2 in N_2) at 850 °C. As can be observed, the performance of the infiltrated backbones is enhanced relative to the non-activated pure NFO–CTO, except for the backbones infiltrated with Al and Nb catalysts. Notably, the Pr-activated electrode shows a significant enhancement, achieving a 10-fold reduction in R_p from 1.85 to 0.17 Ω cm^2 in 21% O_2. Previous studies have demonstrated strong and stable promotion of the oxygen oxidation/reduction reaction (OORR) kinetics by Pr activation, particularly using Pr_6O_{11} nanoparticles infiltrated into the porous backbones.[27,28] Due to this notable effect, Pr-based binary formulations were explored, specifically (i) Ce–Pr in a 1 : 1 molar ratio and (ii) Pr–Al in a 4 : 1 molar ratio. The Ce–Pr oxide binary formulation was selected due to previously reported outstanding catalytic properties,[28,34] while the Pr–Al-based catalyst was selected to combine the beneficial properties of Pr with the acidic character of Al, potentially improving the OORR kinetics under oxyfuel environments due to lower CO_2 and SO_2 adsorption on the active sites. The distinct stoichiometric ratios of Pr–Al and Ce–Pr catalysts were tailored to balance catalytic activity and surface properties, aiming to achieve the optimal OORR performance by compensating for the activity of Al_2O_3 and maximizing the Ce–Pr synergistic effect. As shown in Fig. 2a, both binary catalysts outperform most studied catalysts, although the Pr catalyst still yields the lowest R_p values. The Nyquist and Bode plots depicted in Fig. 2a and b show that the observed R_p reduction in the activated samples is due to a significant lowering of the imaginary component of the impedance at medium and low

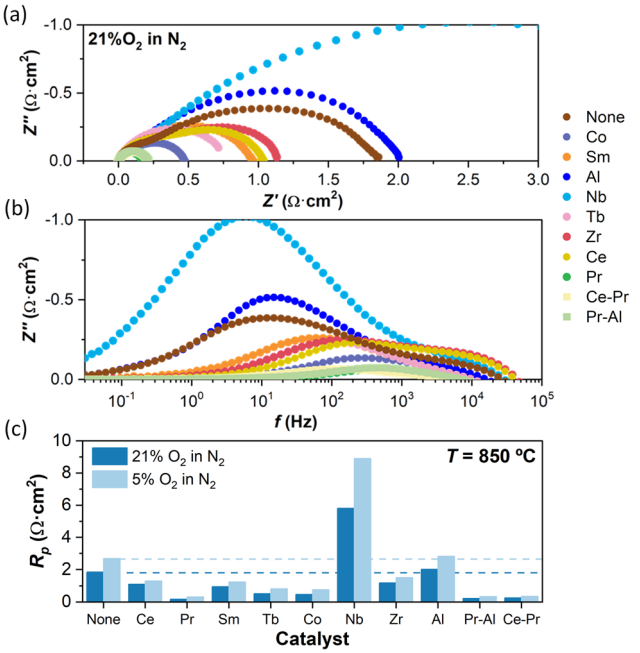

Fig. 2 (a) Nyquist, (b) Bode plots in 21% O_2 in N_2 and (c) Polarization resistance of NFO–CTO backbones, both pure and infiltrated with different catalysts (none, Co, Sm, Al, Nb, Tb, Zr, Ce, Pr, Ce–Pr, and Pr–Al) in 21% O_2 in N_2 and 5% O_2 in N_2, mimicking clean feed and sweep conditions at 850 °C.

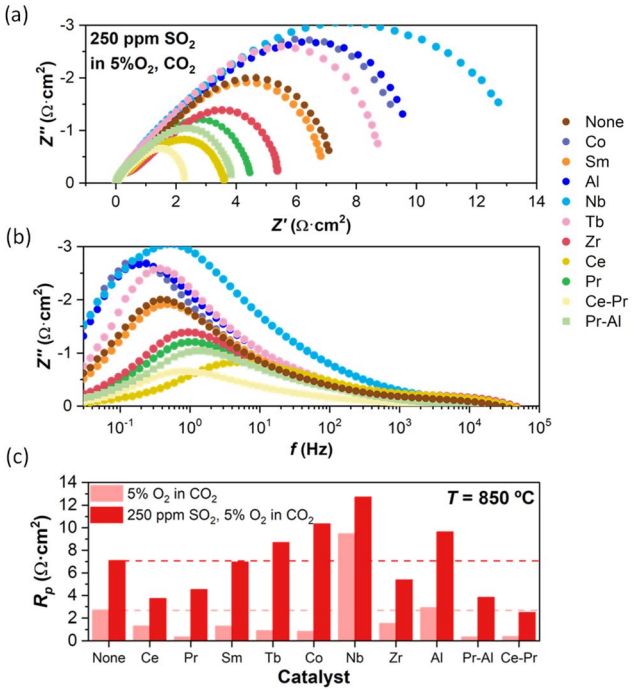

Fig. 3 (a) Nyquist, (b) Bode plots in 250 ppm SO_2, 5% O_2 in CO_2 and (c) polarization resistance of NFO–CTO pure backbones and infiltrated with different catalysts (none, Co, Sm, Al, Nb, Tb, Zr, Ce, Pr, Ce–Pr, and Pr–Al) in 5% O_2 in CO_2 and 250 ppm SO_2, 5% O_2 in CO_2, mimicking oxyfuel conditions at 850 °C.

frequencies (10^{-1}-10^{3} Hz), corresponding to enhanced OORR kinetics at the catalyst surface. Nb and Al catalysts exhibit higher impedance values than pure NFO–CTO in this region, likely due to the lack of redox properties, which hinders oxygen surface exchange. The catalysts producing the most substantial reduction in the R_p values are Pr, Pr–Al, and Ce–Pr. Conversely, pure NFO–CTO and Zr-, Ce-, and Sm-based catalysts exhibit increased impedance contributions at higher frequencies (10^{4} Hz), which may be attributed to partial blocking of pathways for electronic conduction.

Further tests were performed under oxyfuel-like conditions, where the presence of CO_2 and SO_2 is a critical factor, to evaluate performance in such challenging environments. Data of EIS measurements in Fig. 3 show the electrochemical behavior of the different activated backbones under 5% O_2 in CO_2 and 250 ppm SO_2, 5% O_2 in CO_2. Switching the gas atmosphere from 5% O_2 in N_2 (Fig. 2c) to 5% O_2 in CO_2 (Fig. 3c) reveals no significant effect on the R_P values, as shown in Table 2 and Fig. S3 for the pure NFO–CTO backbone. However, exposure to 250 ppm SO_2 during 250 min produces a substantial increase in impedance for all catalytic systems. This increase in R_P occurs at low and medium frequencies (Fig. 3a and b), which is associated with surface-related processes. The observed R_P rise is attributed to SO_2 adsorption on the oxygen active sites, blocking the OORR. Although direct evidence of SO_2 adsorption or sulfate formation (*e.g.*, *via in situ* XPS or DRIFTS) was not performed in this study, the combination of reversible R_P changes, the affected frequency region, and supporting literature provides strong evidence that SO_2 affects the oxygen surface exchange reaction. Despite this detrimental effect, the backbones infiltrated with Zr, Sm, Ce, Pr, Pr–Al, and Ce–Pr catalysts still outperform the non-activated NFO–CTO backbone, with Ce–Pr showing the most pronounced improvement. Specifically, Ce–Pr infiltration reduces the polarization resistance under SO_2 exposure from 7.1 Ω cm^2 (for pure NFO–CTO) to 2.5 Ω cm^2. After SO_2 exposure, the R_p recovery was monitored for 10 h under 5% O_2 in N_2 atmosphere. Table 2 presents the R_p values in 5% O_2 in N_2 before and after SO_2 exposure. The non-activated backbone shows the slightest change in R_p, while the backbones infiltrated with Pr, Tb, Co, and Pr–Al exhibit the largest increases. With the exception of Nb and Al, all infiltrated samples maintain lower R_p values than the pure backbone after the recovery. Notably, Ce–Pr and Ce–Al activated backbones display particularly low R_p values of 0.40 and 0.78 Ω cm^2, respectively, even after SO_2 exposure.

The polarization resistances of the Pr, Ce, Al, Pr–Ce, and Pr–Al activated backbones, as well as the bare NFO–CTO electrode, were obtained by fitting the impedance spectra to an equivalent circuit consisting of three $R\|$CPE elements.[16,24] The resistances at high (R_{HF}), medium (R_{MF}), and low frequencies (R_{LF}) are plotted for the four different studied atmospheres. As shown in Fig. S4, the resistance at HF (>1 kHz) remains almost unaltered across all tested conditions. However, when comparing the measured values of R_{HF} for all catalysts, including the bare material, the highest value of R_{HF} is observed for Ce, Ce–Pr, and the non-infiltrated backbone. This indicates that infiltration of Ce does not enhance the high-frequency performance, which is

Table 2 R_p values obtained from EIS measurements for the different activated backbones under the different conditions tested at 850 °C

	R_p (Ω cm^2)					% R_p var
Catalyst	21% O_2 in N_2	5% O_2 in N_2	5% O_2 in CO_2	250 ppm SO_2	5% O_2 in N_2[a]	5% O_2 in N_2
None	1.85	2.69	2.71	7.09	2.62	−3%
Ce	1.10	1.31	1.33	3.73	1.53	17%
Pr	0.17	0.32	0.35	4.53	1.06	236%
Sm	0.96	1.25	1.31	6.96	2.10	68%
Tb	0.52	0.82	0.91	8.70	1.97	141%
Co	0.47	0.76	0.84	10.34	1.56	103%
Nb	5.81	8.91	9.47	12.72	10.33	16%
Zr	1.19	1.51	1.56	5.38	1.86	23%
Al	2.01	2.82	2.92	9.63	3.35	19%
Pr–Al (4 : 1)	0.22	0.34	0.35	3.83	0.78	132%
Ce–Pr (1 : 1)	0.25	0.35	0.38	2.49	0.40	29%

[a] After being exposed to SO_2.

attributed to the lower conductivity of CeO_2.[35–37] Incorporation of Al_2O_3 increases the resistance at medium frequencies (10–10^3 Hz). Considering that the value of R_{MF} is usually linked with the TPB length, the higher R_{MF} of the Al-infiltrated electrode layer (compared to the bare electrode) can be attributed to the low catalytic activity of Al and, therefore, to the reduction of the TPB length. The limited influence of CO_2 in the inlet stream may indicate negligible competitive adsorption between O_2 and CO_2 at the active sites. Finally, exposure of the activated electrode layers to 250 ppm SO_2 has a pronounced detrimental impact on the polarization resistance at both medium and low frequencies. These frequency regions (<10 Hz) are typically associated with surface and gas-phase diffusion processes.[24,27] The larger size and higher polarizability of SO_2-relative to O_2- facilitate its strong adsorption on active sites, and its dissociation can lead to the formation of sulfate species. These species not only block active sites for oxygen adsorption but also obstruct gas pathways within the porous structure, thereby simultaneously hindering surface exchange reactions and gas diffusion, resulting in a marked increase in polarization resistance.

Overall, the R_P values measured in this work fall within the range reported for state-of-the-art air/O_2 electrode materials, confirming their relevance for application. The invariance of R_P upon switching from O_2/N_2 to O_2/CO_2 indicates superior CO_2 stability compared to BSCF and LSCF, which typically degrade under such conditions.[38,39] Additionally, the materials demonstrated tolerance to SO_2 exposure, indicating robust performance in oxyfuel-relevant environments.

3.3. Pulse isotopic exchange studies

Pulse Isotopic Exchange (PIE) measurements were performed to further investigate the surface electrochemistry of the bare and catalyst-activated NFO–CTO backbones with Pr, Ce, Al, Ce–Pr, and Pr–Al. Fig. 4 shows that the non-activated reference material exhibits a relatively high activation energy of 136 ± 8 kJ mol^{-1}. Infiltration with Pr, a rare earth metal known for its catalytic activity in the OORR, improves the surface exchange rate by more than one order of magnitude. Furthermore, the low activation energy found for the Pr-infiltrated material renders it more suitable for use at intermediate temperatures. In the case of Ce, there is a slight enhancement relative to bare material, which is attributed to the redox properties of CeO_2 nanoparticles.[40,41]

Impregnation of the NFO–CTO composite with Al leads to a two-fold Arrhenius behavior of the surface exchange rate, with a higher activation energy at elevated temperatures. The poor performance observed for the composite after infiltration with Al is expected since alumina (Al_2O_3) exhibits poor catalytic activity for the OORR. The presence of these oxide particles on the composite surface reduces the effective active surface area, thereby reducing the surface exchange rate. Conversely, samples impregnated with binary catalysts, Ce–Pr or Pr–Al, show a substantial increase in the exchange rates, consistent with the trends observed in the EIS measurements. For comparison, PIE data of reference materials including BSFC, STF35, GDC, LSCF, and LSC20 are also presented in Fig. S5,

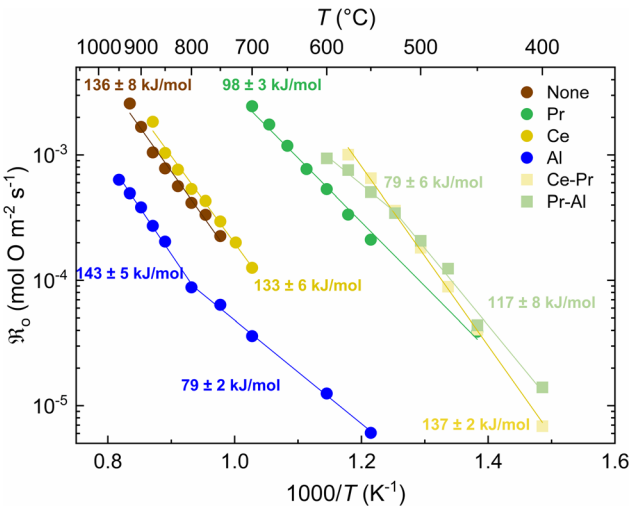

Fig. 4 Surface exchange rate of non-activated and activated NFO–CTO composite powders as a function of inverse temperature.

allowing a direct assessment of the composites studied to commonly investigated OTM and solid-oxide electrochemical cells (SOC) materials. The results indicate that the investigated composites exhibit surface exchange kinetics and activation energies within the range reported for leading OTM/SOC candidates, underscoring their potential applicability in oxygen transport and electrochemical devices.[42–44]

3.4. Oxygen permeation studies

Oxygen permeation tests were conducted on 0.6 mm-thick NFO–CTO membranes (bare), coated with a 30 μm-thick porous NFO–CTO backbone (none), and infiltrated with Pr, Ce, Al, Ce–Pr, and Pr–Al catalysts. The O_2 permeation was studied under an air/Ar gradient in the temperature range from 850 to 700 °C. The evolution of the oxygen flux, $J(O_2)$, with temperature for the different activated cases is depicted in Fig. 5a. The addition of a porous NFO–CTO layer enhances $J(O_2)$ by a factor of 2.5 at 850 °C, which is even more significant as the temperature is lowered. Several publications have reported an increase in the permeation by surface modification.[45,46] This enhancement can be ascribed to the increase in the membrane surface specific area and, thus, to the formation of additional active sites for oxygen exchange. The infiltration of Ce, Pr, and the binary combinations Ce–Pr and Pr–Al into the porous NFO–CTO backbones increases $J(O_2)$. Conversely, $J(O_2)$ decreases after activation with Al, consistent with its poor catalytic activity for the oxygen surface exchange reaction The results in Fig. 5a show that the most significant improvement in flux is obtained after activation with Ce–Pr, resulting in a 6-fold increase of $J(O_2)$, at 850 °C, relative to the non-infiltrated NFO–CTO-coated membrane. These results are in excellent agreement with data from EIS and PIE, confirming the role of the catalyst nanoparticle in activation of the OORR and the importance of the surface exchange reactions in governing O_2 permeation at temperatures below 850 °C.

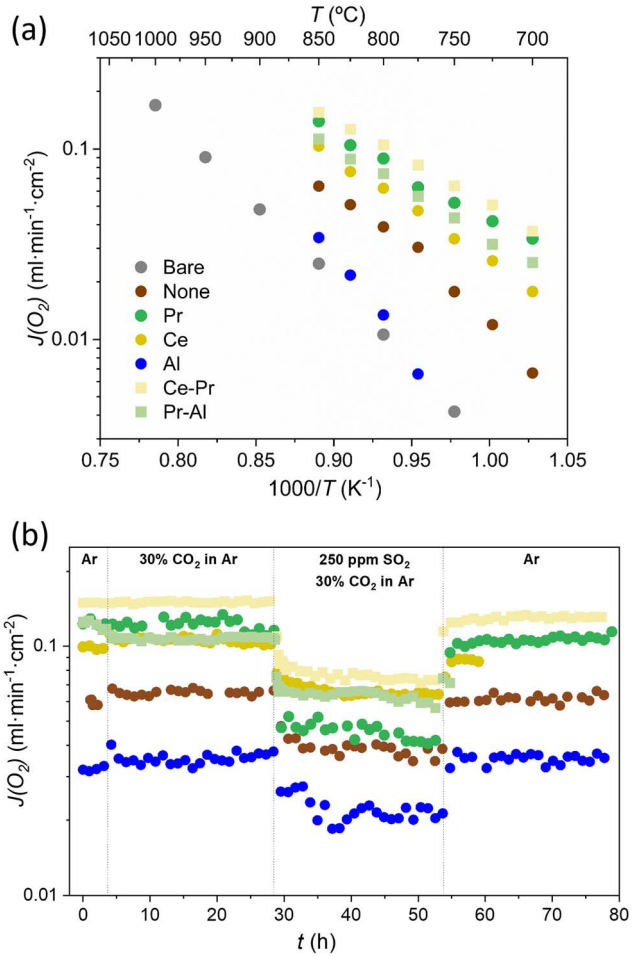

Fig. 5 (a) Oxygen permeation of NFO–CTO membranes (bare), coated with an NFO–CTO backbone (none), and infiltrated with Pr, Ce, Al, Ce–Pr, and Pr–Al catalysts in dependence on temperature (Q_{feed} = 100 ml min^{-1}, Q_{sweep} = 150 ml min^{-1}). (b) Oxygen permeation evolution in dependence on time of different activated membranes under different sweep environments involving CO_2 and SO_2 (Q_{feed} = 100 ml min^{-1}, Q_{sweep} = 150 ml min^{-1}) at 850 °C.

In view of the above results, Ce, Pr, Pr–Al, and Ce–Pr catalysts are identified as most promising for catalytic activation of membranes subjected to oxyfuel environments. Short-term stability tests of 24 h were performed on NFO–CTO activated membranes by monitoring the evolution of $J(O_2)$ under different environments at the sweep side (Argon, 30% CO_2 in Argon, 250 ppm SO_2 in 30% CO_2 in Argon) while feeding with synthetic air at 850 °C. The results in Fig. 5b demonstrate stable behavior for the coated NFO–CTO membrane under all tested conditions. A slight drop in $J(O_2)$ is observed under SO_2-containing environment, but the flux recovers slowly to its initial value when switching back to clean conditions. This recovery demonstrates the stability of NFO–CTO in oxyfuel atmospheres and indicates that the performance loss is due to SO_2 adsorption, which hinders the oxygen surface exchange reaction without causing permanent structural degradation.

The activation of the NFO–CTO-coated membrane with Al yields lower $J(O_2)$ across all conditions used in this study, confirming its poor activity in the OORR. In contrast, all other catalysts enhance performance under the given conditions, as expected. Among them, the Ce–Pr catalyst yields the highest

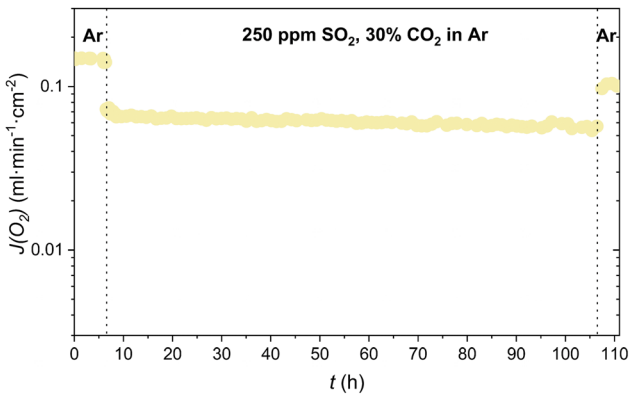

Fig. 6 Oxygen permeation evolution over time for the Ce–Pr activated membrane under different sweep environments involving CO_2 and SO_2 (Q_{feed} = 100 ml min^{-1}, Q_{sweep} = 150 ml min^{-1}) at 850 °C.

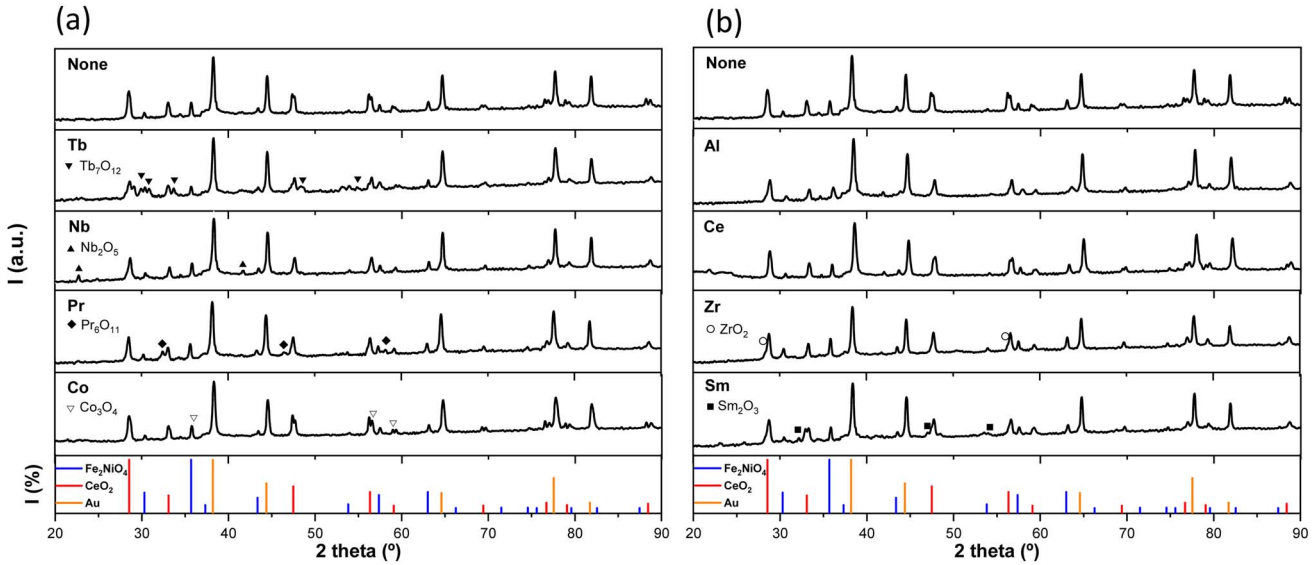

Fig. 7 XRD patterns of the NFO–CTO backbones, non-activated (none) and activated (a) Tb, Nb, Pr, Co, and (b) Al, Ce, Zr, and Sm layers after the EIS tests performed in O_2, CO_2, and SO_2 environments.

oxygen flux, reaching 0.15 and 0.07 ml min^{-1} cm^{-2} under CO_2 and SO_2 conditions, respectively. This represents a 2.5-fold improvement with respect to the non-infiltrated NFO–CTO membrane under the same harsh conditions. The Ce and Pr–Al catalysts perform exceptionally well when exposed to SO_2-containing atmospheres.

Finally, a long-term stability test was conducted using a Ce–Pr-activated NFO–CTO membrane for 100 h at 850 °C. Fig. 6 depicts the oxygen flux when exposed to 250 ppm SO_2, 30% CO_2 in Argon. As can be seen when switching from clean conditions to a sweep gas containing SO_2, $J(O_2)$ drops to 0.07 ml min^{-1} cm^{-2}. Next, $J(O_2)$ declines at a constant rate of 0.00013 ml $min^{-1}\cdot cm^{-2}$ (0.14%) per hour, reaching a value of 0.057 ml $min^{-1}\cdot cm^{-2}$ after 100 h. After the stability test, the feed was switched again to clean Ar sweeping conditions, reaching a value of $J(O_2)$ of 0.11 ml $min^{-1}\cdot cm^{-2}$ after 5 h with a slow flux recovery, which is lower than the initial value of 0.15 ml $min^{-1}\cdot cm^{-2}$ before SO_2 exposure. This type of degradation and recovery determined by SO_2 desorption kinetics has also been observed for other spinel/fluorite membranes.[16,47]

3.5. Post-mortem characterization

XRD analysis of the symmetrical cells was conducted after EIS measurements were performed in O_2, CO_2, and SO_2 environments on both the non-activated and activated porous NFO–CTO backbones. The diffraction patterns correspond to the peaks associated with the NFO–CTO phase (porous layer) and the different oxide catalysts (none, Tb_7O_{12}, Nb_2O_3, Co_3O_4, Pr_6O_{11}, Sm_2O_3, ZrO_2, CeO_2, Al_2O_3). The Au signal is due to the gold contacts used as current collectors. No sulfates were detected after SO_2 exposure (Fig. 7), suggesting that the irreversible performance loss observed in the membranes may be attributed to the formation of minor phases or to catalyst nanoparticles coarsening during time on stream.

A SEM image of a fresh NFO–CTO membrane coated with a porous NFO–CTO backbone infiltrated with Ce–Pr (Fig. 8) is

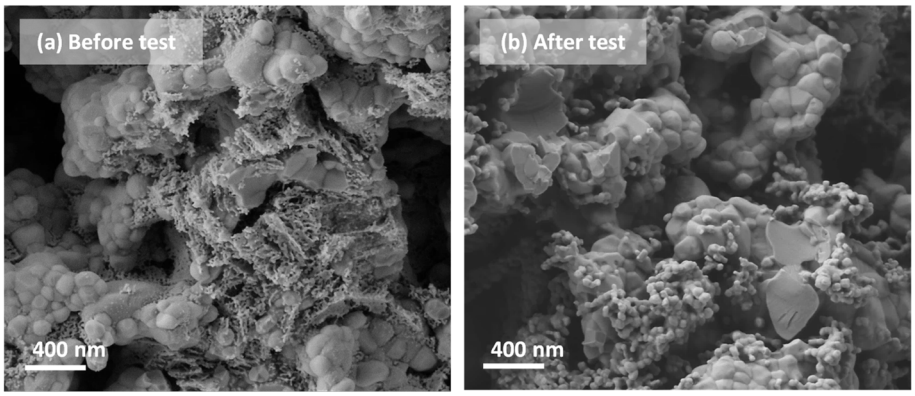

Fig. 8 SEM images of the NFO–CTO membrane coated with a porous NFO–CTO backbone infiltrated with Ce–Pr (a) before and (b) after the 100 h oxygen permeation stability test with SO_2 and CO_2 atmospheres.

compared with the same cell after the 100 h oxygen permeation stability test in SO_2- and CO_2-containing atmospheres. The post-test images reveal a loss of catalyst dispersion and significant particle growth, which likely contribute to the performance degradation over time, particularly the reduced $J(O_2)$ observed upon returning to clean conditions. EDX post-mortem analysis on the tested sample (Fig. S6) reveals no formation of sulfur species, either in the catalytic layer or on the membrane surface exposed to SO_2, thus confirming the chemical stability of NFO–CTO and CeO_x–PrO_x after long-term CO_2 and SO_2 exposure.

4. Conclusions

Targeted catalyst activation strategies enabled a substantial enhancement in the performance of Fe_2NiO_4–$Ce_{0.8}Tb_{0.2}O_{2-\delta}$ (NFO–CTO) membranes for high-temperature oxygen separation applications. Various oxide catalysts, comprising individual lanthanides (Ce, Pr, Tb, Sm), transition metals (Co, Nb, Al, Zr), and binary combinations (Ce–Pr and Pr–Al), were systematically screened with the aim of enhancing the oxygen surface exchange kinetics. Through comprehensive electrochemical characterization using electrochemical impedance spectroscopy (EIS) and pulsed isotopic exchange (PIE) techniques, Pr, Ce, Pr–Al, and Ce–Pr were consistently identified as the most effective catalyst systems. These activations significantly enhanced the oxygen surface exchange reaction, correlating with improvements in the overall membrane performance. Activation of the porous NFO–CTO membrane overlayers with Pr, in particular, yielded a 10-fold reduction in the polarization resistance, decreasing from 1.85 Ω cm^2 to 0.17 Ω cm^2 in air. Under simulated combustion environments containing 250 ppm SO_2 and CO_2, Ce–Pr activation demonstrated the highest activity and stability, achieving an R_p of 2.49 Ω cm^2. Oxygen permeation measurements further supported the electrochemical findings, with Pr-, Ce-, Pr–Al-, and Ce–Pr-activated membranes consistently exhibiting the highest oxygen fluxes. Under clean conditions at 850 °C, a six-fold increase in oxygen production was achieved with Ce–Pr activation, while a 2.5-fold improvement was observed under harsh SO_2/CO_2 conditions. Long-term stability tests conducted over 100 h indicated low performance degradation, with a sustained oxygen flux decline of only 0.14% per hour. Microstructural analysis suggested that the degradation mechanisms were primarily associated with nanoparticle coarsening and partial loss of catalyst dispersion.

These results highlight the critical role of tailored catalyst activation in simultaneously improving the activity and durability of mixed ionic–electronic conducting membranes for high-temperature oxygen separation technologies. Under oxy-fuel conditions, achieving high oxygen permeation requires not only the enhancement of surface exchange kinetics but also robust resistance against performance degradation caused by gases present in oxyfuel conditions, such as CO_2 and SO_2. In this study, the NFO–CTO membrane was used as a model material, and the insights gained were applied to the design and selection of catalyst activation strategies. The resulting membranes exhibit high catalytic activity combined with excellent stability under harsh CO_2/SO_2-containing environments. These findings are expected to be transferable to other dual-phase composite systems.

Conflicts of interest

There are no conflicts to declare.

Data availability

The data supporting this article have been included as part of the supplementary information (SI). Supplementary information: XRD patterns, Nyquist and Bode plots, EIS-derived resistance contributions, surface exchange rates compared with benchmark materials, and EDX analyses of NFO–CTO membranes activated with various catalysts. See DOI: **https://doi.org/10.1039/d5ta06504f**.

Acknowledgements

Financial support from the Spanish Government (PID2022-139663OB-100 and CEX2021-001230-S grant funded by MCIN/AEI/10.13039/501100011033) and the Generalitat Valenciana (CIPROM/2022/10) is also acknowledged. Financial support by the EU through FP7 GREEN-CC Project (Grant Agreement Number: 608524). We thank the support of the Electronic Microscopy Service of the Universitat Politècnica de València.

Notes and references

1 H. Barlow, S. S. M. Shahi and M. Loughrey, *State Of The Art: CCS Technologies 2023*, 2023. **https://www.globalccsinstitute.com/resources/publications-reports-research/state-of-the-art-ccs-technologies-2023/**, accessed September 25, 2023.

2 W. Gao, S. Liang, R. Wang, Q. Jiang, Y. Zhang, Q. Zheng, B. Xie, C. Y. Toe, X. Zhu, J. Wang, L. Huang, Y. Gao, Z. Wang, C. Jo, Q. Wang, L. Wang, Y. Liu, B. Louis, J. Scott, A. C. Roger, R. Amal, H. He and S. E. Park, Industrial carbon dioxide capture and utilization: State of the art and future challenges, *Chem. Soc. Rev.*, 2020, **49**, 8584–8686, DOI: **10.1039/d0cs00025f**.

3 I. – International Energy Agency, *Electricity 2024 – Analysis and forecast to 2026*, 2024. **https://www.iea.org/reports/electricity-2024**, accessed February 12, 2025.

4 D. Y. C. Leung, G. Caramanna and M. M. Maroto-Valer, An overview of current status of carbon dioxide capture and storage technologies, *Renewable Sustainable Energy Rev.*, 2014, **39**, 426–443, DOI: **10.1016/j.rser.2014.07.093**.

5 A. F. Ghoniem, *Energy Conversion Engineering: Towards Low CO2 Power and Fuels*, Cambridge University Press, 2021, **https://books.google.es/books?id=sh5MEAAAQBAJ**.

6 A. C. Bose, *Inorganic Membranes for Energy and Environmental Applications*, Springer New York, New York, NY, 2009, DOI: **10.1007/978-0-387-34526-0**.

7 M. A. Habib, H. M. Badr, S. F. Ahmed, R. Ben-Mansour, K. Mezghani, S. Imashuku, G. J. la O', Y. Shao-Horn,

N. D. Mancini, A. Mitsos, P. Kirchen and A. F. Ghoneim, A review of recent developments in carbon capture utilizing oxy-fuel combustion in conventional and ion transport membrane systems, *Int. J. Energy Res.*, 2011, **35**, 741–764, DOI: 10.1002/er.1798.

8 S. S. Hashim, A. R. Mohamed and S. Bhatia, Oxygen separation from air using ceramic-based membrane technology for sustainable fuel production and power generation, *Renewable Sustainable Energy Rev.*, 2011, **15**, 1284–1293, DOI: 10.1016/j.rser.2010.10.002.

9 R. J. Allam, Improved oxygen production technologies, *Energy Procedia*, 2009, **1**, 461–470, DOI: 10.1016/j.egypro.2009.01.062.

10 N. F. Himma, A. K. Wardani, N. Prasetya, P. T. P. Aryanti and I. G. Wenten, Recent progress and challenges in membrane-based O_2/N_2 separation, *Rev. Chem. Eng.*, 2019, **35**, 591–625, DOI: 10.1515/revce-2017-0094.

11 P. Markewitz, J. Marx, A. Schreiber and P. Zapp, Ecological evaluation of coal-fired oxyfuel power plants-cryogenic *versus* membrane-based air separation, in *Energy Procedia*, Elsevier Ltd, 2013, pp. 2864–2876. doi: DOI: 10.1016/j.egypro.2013.06.172.

12 H. Luo, T. Klande, Z. Cao, F. Liang, H. Wang and J. Caro, A CO_2-stable reduction-tolerant Nd-containing dual phase membrane for oxyfuel CO_2 capture, *J. Mater. Chem. A*, 2014, **2**, 7780–7787, DOI: 10.1039/c3ta14870j.

13 X. Zhu, H. Liu, Y. Cong and W. Yang, Novel dual-phase membranes for CO_2 capture *via* an oxyfuel route, *Chem. Commun.*, 2012, **48**, 251–253, DOI: 10.1039/C1CC16631J.

14 K. S. Yun, C.-Y. Yoo, S.-G. Yoon, J. H. Yu and J. H. Joo, Chemically and thermo-mechanically stable LSM–YSZ segmented oxygen permeable ceramic membrane, *J. Membr. Sci.*, 2015, **486**, 222–228, DOI: 10.1016/j.memsci.2015.03.049.

15 R. Kiebach, S. Pirou, L. Martinez Aguilera, A. B. Haugen, A. Kaiser, P. V. Hendriksen, M. Balaguer, J. García-Fayos, J. M. Serra, F. Schulze-Küppers, M. Christie, L. Fischer, W. A. Meulenberg and S. Baumann, A review on dual-phase oxygen transport membranes: from fundamentals to commercial deployment, *J. Mater. Chem. A*, 2022, **10**, 2152–2195, DOI: 10.1039/d1ta07898d.

16 M. Laqdiem, J. Garcia-Fayos, A. J. Carrillo, L. Almar, M. Balaguer, M. Fabuel and J. M. Serra, Co_2MnO_4/$Ce_{0.8}Tb_{0.2}O_{2-\delta}$ Dual-Phase Membrane Material with High CO_2 Stability and Enhanced Oxygen Transport for Oxycombustion Processes, *ACS Appl. Energy Mater.*, 2024, **7**, 302–311, DOI: 10.1021/acsaem.3c02606.

17 C. Gaudillere, J. Garcia-Fayos, M. Balaguer and J. M. Serra, Enhanced Oxygen Separation through Robust Freeze-Cast Bilayered Dual-Phase Membranes, *ChemSusChem*, 2014, **7**, 2554–2561, DOI: 10.1002/cssc.201402324.

18 J. Garcia-Fayos, M. Balaguer and J. M. Serra, Dual-Phase Oxygen Transport Membranes for Stable Operation in Environments Containing Carbon Dioxide and Sulfur Dioxide, *ChemSusChem*, 2015, **8**, 4242–4249, DOI: 10.1002/cssc.201500951.

19 M. Balaguer, J. García-Fayos, C. Solís and J. M. Serra, Fast Oxygen Separation Through SO_2 - and CO_2-Stable Dual-Phase Membrane Based on $NiFe_2O_4$–$Ce_{0.8}Tb_{0.2}O_{2-\delta}$, *Chem. Mater.*, 2013, **25**, 4986–4993, DOI: 10.1021/cm4034963.

20 W. Fang, F. Steinbach, C. Chen and A. Feldhoff, An Approach To Enhance the CO_2 Tolerance of Fluorite-Perovskite Dual-Phase Oxygen-Transporting Membrane, *Chem. Mater.*, 2015, **27**, 7820–7826, DOI: 10.1021/acs.chemmater.5b03823.

21 Z. Wang, H. Liu, X. Tan, Y. Jin and S. Liu, Improvement of the oxygen permeation through perovskite hollow fibre membranes by surface acid-modification, *J. Membr. Sci.*, 2009, **345**, 65–73, DOI: 10.1016/j.memsci.2009.08.024.

22 Y. Wei, Q. Liao, Z. Li and H. Wang, Enhancement of oxygen permeation through U-shaped K_2NiF_4-type oxide hollow fiber membranes by surface modifications, *Sep. Purif. Technol.*, 2013, **110**, 74–80, DOI: 10.1016/j.seppur.2013.03.006.

23 H. Bouwmeester and P. Gellings, *Handbook of Solid State Electrochemistry*, CRC Press, 1997, DOI: 10.1201/9781420049305.

24 M. Laqdiem, J. Garcia-Fayos, L. Almar, M. Balaguer and J. M. Serra, The role of ionic-electronic ratio in dual-phase catalytic layers for oxygen transport permeation membranes, *J. Membr. Sci.*, 2023, **676**, 121578, DOI: 10.1016/j.memsci.2023.121578.

25 J. H. Joo, K. S. Yun, J.-H. Kim, Y. Lee, C.-Y. Yoo and J. H. Yu, Substantial Oxygen Flux in Dual-Phase Membrane of Ceria and Pure Electronic Conductor by Tailoring the Surface, *ACS Appl. Mater. Interfaces*, 2015, **7**, 14699–14707, DOI: 10.1021/acsami.5b03392.

26 Y. Il Kwon, J. H. Park, S. M. Kang, G. D. Nam, J. W. Lee, J. H. Kim, D. Kim, S. M. Jeong, J. H. Yu and J. H. Joo, Novel strategy for improving the oxygen permeability of zirconia-based dual-phase membranes, *Energy Environ. Sci.*, 2019, **12**, 1358–1368, DOI: 10.1039/c8ee03105c.

27 L. Navarrete, C. Solís and J. M. Serra, Boosting the oxygen reduction reaction mechanisms in IT-SOFC cathodes by catalytic functionalization, *J. Mater. Chem. A*, 2015, **3**, 16440–16444, DOI: 10.1039/c5ta05187h.

28 J. García-Fayos, R. Ruhl, L. Navarrete, H. J. M. Bouwmeester and J. M. Serra, Enhancing oxygen permeation through Fe_2NiO_4-$Ce_{0.8}Tb_{0.2}O_{2-\delta}$ composite membranes using porous layers activated with Pr_6O_{11} nanoparticles, *J. Mater. Chem. A*, 2018, **6**, 1201–1209, DOI: 10.1039/c7ta06485c.

29 C. Nicollet, C. Toparli, G. F. Harrington, T. Defferriere, B. Yildiz and H. L. Tuller, Acidity of surface-infiltrated binary oxides as a sensitive descriptor of oxygen exchange kinetics in mixed conducting oxides, *Nat. Catal.*, 2020, **3**, 913–920, DOI: 10.1038/s41929-020-00520-x.

30 M. Balaguer, C. Solís, S. Roitsch and J. M. Serra, Engineering microstructure and redox properties in the mixed conductor $Ce_{0.9}Pr_{0.1}O_{2-\delta}$ + Co 2 mol%, *Dalton Trans.*, 2014, **43**, 4305–4312, DOI: 10.1039/c3dt52167b.

31 M. Balaguer, C. Solís and J. M. Serra, Study of the transport properties of the mixed ionic electronic conductor $Ce_{1-x}Tb_xO_{2-\delta}$ + Co (x = 0.1, 0.2) and evaluation as oxygen-

transport membrane, *Chem. Mater.*, 2011, **23**, 2333–2343, DOI: 10.1021/cm103581w.

32 C. Solís, M. Balaguer, F. Bozza, N. Bonanos and J. M. Serra, Catalytic surface promotion of highly active $La_{0.85}Sr_{0.15}Cr_{0.8}Ni_{0.2}O_{3-\delta}$ anodes for $La_{5.6}WO_{11.4-\delta}$ based proton conducting fuel cells, *Appl. Catal., B*, 2014, **147**, 203–207, DOI: 10.1016/j.apcatb.2013.08.044.

33 H. J. M. Bouwmeester, C. Song, J. Zhu, J. Yi, M. Van Sint Annaland and B. A. Boukamp, A novel pulse isotopic exchange technique for rapid determination of the oxygen surface exchange rate of oxide ion conductors, *Phys. Chem. Chem. Phys.*, 2009, **11**, 9640–9643, DOI: 10.1039/b912712g.

34 S. Pirou, J. García-Fayos, M. Balaguer, R. Kiebach and J. M. Serra, Improving the performance of oxygen transport membranes in simulated oxy-fuel power plant conditions by catalytic surface enhancement, *J. Membr. Sci.*, 2019, **580**, 307–315, DOI: 10.1016/j.memsci.2019.03.027.

35 R. G. Biswasr, M. Rajendran, G. S. Walker, E. Williams and A. K. Bhattacharyas, *Electrical transport studies and temperature-programmed oxygen evolution of PrO 1.83*, 1998.

36 S. Ferro, Physicochemical and Electrical Properties of Praseodymium Oxides, *Int. J. Electrochem.*, 2011, **2011**, 1–7, DOI: 10.4061/2011/561204.

37 M. Balaguer, C. Solís and J. M. Serra, Structural-transport properties relationships on $Ce_{1-x}Ln_xO_{2-\delta}$ system (Ln = Gd, La, Tb, Pr, Eu, Er, Yb, Nd) and effect of cobalt addition, *J. Phys. Chem. C*, 2012, **116**, 7975–7982, DOI: 10.1021/jp211594d.

38 M. Pagliari, D. Montinaro, E. Martelli, S. Campanari and A. Donazzi, Durability and kinetic effects of CO_2-rich oxidizing streams on LSCF-based solid oxide fuel cells, *J. Power Sources*, 2024, **613**, 234895, DOI: 10.1016/J.JPOWSOUR.2024.234895.

39 L. Almar, H. Störmer, M. Meffert, J. Szász, F. Wankmüller, D. Gerthsen and E. Ivers-Tiffée, Improved Phase Stability and CO_2 Poisoning Robustness of Y-Doped $Ba_{0.5}Sr_{0.5}Co_{0.8}Fe_{0.2}O_{3-\delta}$ SOFC Cathodes at Intermediate Temperatures, *ACS Appl. Energy Mater.*, 2018, **1**, 1316–1327, DOI: 10.1021/acsaem.8b00028.

40 X. Lin, L. Zhou, T. Huang and A. Yu, Cerium Oxides as Oxygen Reduction Catalysts for Lithium-Air Batteries, *Int. J. Electrochem. Sci.*, 2012, **7**, 9550–9559, DOI: 10.1016/S1452-3981(23)16218-3.

41 G. R. Rao and B. G. Mishra, *Structural, Redox And Catalytic Chemistry of Ceria Based Materials*, 2003.

42 C. Y. Yoo, B. A. Boukamp and H. J. M. Bouwmeester, Oxygen surface exchange kinetics of erbia-stabilized bismuth oxide, *J. Solid State Electrochem.*, 2011, **15**, 231–236, DOI: 10.1007/S10008-010-1168-8.

43 C. Y. Yoo and H. J. M. Bouwmeester, Oxygen surface exchange kinetics of $SrTi_{1-x}Fe_xO_{3-\delta}$ mixed conducting oxides, *Phys. Chem. Chem. Phys.*, 2012, **14**, 11759–11765, DOI: 10.1039/C2CP41923H.

44 H. J. M. Bouwmeester, C. Song, J. Zhu, J. Yi, M. Van Sint Annaland and B. A. Boukamp, A novel pulse isotopic exchange technique for rapid determination of the oxygen surface exchange rate of oxide ion conductors, *Phys. Chem. Chem. Phys.*, 2009, **11**, 9640–9643, DOI: 10.1039/B912712G.

45 J. M. Serra, J. Garcia-Fayos, S. Baumann, F. Schulze-Küppers and W. A. Meulenberg, Oxygen permeation through tape-cast asymmetric all-$La_{0.6}Sr_{0.4}Co_{0.2}Fe_{0.8}O_{3-\delta}$ membranes, *J. Membr. Sci.*, 2013, **447**, 297–305, DOI: 10.1016/j.memsci.2013.07.030.

46 C. Gaudillere, J. Garcia-Fayos and J. M. Serra, Oxygen Permeation Improvement under CO_2-Rich Environments through Catalytic Activation of Hierarchically Structured Perovskite Membranes, *Chempluschem*, 2014, **79**, 1720–1725, DOI: 10.1002/cplu.201402142.

47 M. Ramasamy, E. S. Persoon, S. Baumann, M. Schroeder, F. Schulze-Küppers, D. Görtz, R. Bhave, M. Bram and W. A. Meulenberg, Structural and chemical stability of high performance $Ce_{0.8}Gd_{0.2}O_{2-\delta}$–$FeCo_2O_4$ dual phase oxygen transport membranes, *J. Membr. Sci.*, 2017, **544**, 278–286, DOI: 10.1016/J.MEMSCI.2017.09.011.

